Electronic Supplementary Information

A highly soluble, crystalline, covalent organic framework compatible with device implementation

Lingling Wang, Cheng Zeng, Hong Xu, Panchao Yin, Dongcheng Chen, Jian Deng, Mu Li, Nan Zheng, Cheng Gu, and Yuguang Ma**

Table of Contents

Supplementary Materials and Methods

Materials and synthetic procedures

Mesitylene, chloroform, methanol, ethanol, THF, anhydrous dioxane, and anhydrous acetone (99.5%) were purchased from Aldrich. NMP, DMI, DMF, DEF, DMSO and DMAc were purchased from TCI. 1,1'-Bis(4-formylphenyl)-[4,4'-bipyridine]-1,1'-diium chloride and 4,4',4'',4'''-(pyrene-1,3,6,8-tetrayl)tetraaniline were prepared using literature procedures[S1,S2].

Synthesis of the PyVg-COF. A mixture of 4,4',4'',4'''-(pyrene-1,3,6,8-tetrayl)tetraaniline (8 mg) and 1,1'-bis(4-formylphenyl)-[4,4'-bipyridine]-1,1'-diium chloride (12.3 mg) in DMAc/mesitylene/6 M AcOH (1.1 mL, 1/9/1 v/v) in a 10 mL Pyrex tube was degassed through three freeze-pump-thaw cycles. The tube was sealed and heated at 120 °C for 7 days. The resulting precipitate was collected by centrifugation, subjected to Soxhlet extraction with anhydrous acetone, methanol and THF for 12 h for each solvent, and then was dried to produce the PyVg-COF (7.5 mg) in a 38% isolated yield as a brownish-red powder.

Preparation of the PyVg-COF solutions and films. The PyVg-COF solutions were prepared by adding PyVg-COF powders to various organic solvents, such as NMP, DMF, DMSO, DEF, DMAc, and DMI, followed by simple manual shaking. More concentrated solutions could be prepared by slight ultrasonication of the COF-solvent mixtures for 1 to 5 minutes. The PyVg-COF nanosheet films were prepared by drop-casting the above solutions onto the desired substrate followed by thermal evaporation of the solvents, which afforded continuous and high-quality films.

Synthesis of COF films by an EPD method. The COF films on electrodes were synthesised by EPD of the PyVg-COF (4.9 mg mL^{-1}) in a two-electrode system using ITO, gold, or stainless steel as the working and counter electrodes with DMI as the solvent at 25 °C. The EPD was conducted by applying a constant DC voltage, and the film thickness was controlled by regulating the applied voltage and the EPD time. After EPD, the films were washed with acetonitrile to remove the DMI, dried under flowing Ar and stored in a glove box in the dark.

Methods.

^{1}H and ^{13}C NMR spectra were recorded on a Bruker AVANCE HD III 500M NMR spectrometer, where the chemical shifts (δ in ppm) were determined with respect to tetramethylsilane (TMS) as an internal reference. Fourier transform Infrared (FT-IR) spectra were recorded on an IFS 66V/S Fourier transform infrared spectrophotometer. UV-Vis spectra were recorded on a Shimadzu UV-3600 spectrometer. The PXRD data for the structural analyses of PyVg-COF were collected using a synchrotron X-ray and multiple PILATUS 100K detectors of the BL5S2 beam line (λ = 0.79964 Å) at Aichi Synchrotron Radiation Center. The crystalline powder of PyVg-COF in a silica glass capillary (0.4 mm inside diameter) was heated at 393 K in vacuum for 1 h to remove the guest molecules. The sample for the structural analysis of PyVg-COF was sealed in vacuum. Elemental analysis was performed on an Elementar Vario EL elemental analyser. TGA measurements were performed on a Rigaku Thermo plus EVO2 under N_2, by heating to 800 °C at a rate of 5 °C min^{-1}. Field-emission scanning electron microscopy (FE-SEM) was performed on a Zeiss_Merlin operating at an accelerating voltage of 5.0 kV. The sample was prepared by drop-casting an NMP solution onto mica substrate followed by thermal evaporation and then coated with platinum. High-resolution transmission electron microscopy (HR-TEM) images were obtained on a TEM JEOL 2100F with an acceleration voltage of 300 kV. Photoluminescence spectra were recorded on a Jobin-Yvon Spex Fluorolog-3 spectrofluorometer. Atomic force microscopy (AFM) measurement was carried out using a Digita Instrumental DI Multimode Nanoscope IIIa in taping mode. Electron paramagnetic resonance (EPR) spectra were measured on Bruker E500 electron paramagnetic resonance spectrometer. The film thickness was recorded on a Veeco Dektak 150 atomic profiler. Grazing-incidence wide-angle X-ray scattering (GIWAXS) experiments were carried out on a Xenocs Xeuss 2.0 system with an Excillum MetalJet-D2 X-ray source operated at 70.0 kV, 2.8570 mA, and a wavelength of 1.341 Å. The grazing-incidence angle was set at 0.20°. Scattering pattern was collected with a DECTRIS PILATUS3 R 1M area detector.

Theoretical simulation.

The crystalline structures of PyVg-COF were determined using the density-functional tight-binding (DFTB)[S3]. The calculations were carried out with the DFTB+ program package version 17.1[S4]. DFTB[S5] is an approximate density functional theory method based on the tight binding approach and utilises an optimised minimal LCAO Slater-type all-valence basis set in combination with a two-center approximation for Hamiltonian matrix elements. The Coulombic interaction between partial atomic charges was determined using the self-consistent charge (SCC) formalism. The lattice dimensions were optimised simultaneously with the geometry. Standard DFTB parameters for X–Y element pair (X, Y = C, H, N and Cl) interactions were employed from the 3ob set[S5–S8]. Discovery Studio Visualizer were employed to build inputting files for DFTB simulation and visualise simulating results[S9].

The adsorption energy was calculated using spin-polarised DFT method with periodic boundary conditions as implemented in the Vienna Ab initio Simulation Package (VASP 5.4.1)[S10,S11]. The Perdew-Burke-Ernzerhof functional[S12] with Grimme's semiempirical "D3" dispersion term[S13] (PBE-D3) was employed in these calculations. Plane wave basis sets with an energy cutoff of 500 eV were used to describe valence electrons, while core electrons were described by the projector-augmented-wave pseudopotentials[S14,S15]. The Brillouin zone was sampled by a Γ-point. During the geometry optimisation, both cell parameters and atomic positions were fully optimised until all atomic forces become smaller than 0.01 eV/Å.

Gas sorption measurements.

Gas sorption isotherms were measured on a BELSORP-max (MicrotracBEL, Japan, Corp.) automated volumetric sorption analyser, equipped with cryostatic temperature controllers. Before measurement, the samples were degassed in vacuum at 120 °C for 11 h. By using the non-local density functional theory (NLDFT) model, the pore volume was derived from the sorption curve.

IAST calculations.

The selectivity of preferential adsorption of component 1 over component 2 in a mixture containing 1 and 2, perhaps in the presence of other components too, can be formally defined as

$$S_{ads} = \frac{q_1/q_2}{p_1/p_2} \qquad (1)$$

In equation (1), q_1 and q_2 are the absolute component loadings of the adsorbed phase in the mixture. These component loadings are also termed the uptake capacities. In all the calculations to be presented below, the calculations of q_1 and q_2 are based on the use of the Ideal Adsorbed Solution Theory (IAST) of Myers and Prausnitz[S16]. The accuracy of the IAST calculations for estimation of the component loadings for several binary mixtures in a wide variety of zeolites and MOFs has been established by comparison with Configurational-Bias Monte Carlo (CBMC) simulations of mixture adsorption[S17–S19].

Isosteric heat of adsorption.

The binding energy of CO_2 is reflected in the isosteric heat of adsorption, Q_{st}, defined as

$$Q_{st} = RT^2 \left(\frac{\partial \ln p}{\partial T} \right)_q \tag{2}$$

The calculations are based on the use of the Clausius−Clapeyron equation.

Small Angle Neutron Scattering (SANS) Measurements.

SANS measurements were carried out in *Suanni* instrument at the 20 MW China Mianyang Research Reactor (CMRR) in China Academy of Engineering Physics (CAEP) in Sichuan, China. The wavelength of neutron source was 5.3 Å (Δλ/λ ~ 10%). Samples were prepared by dissolving 6 mg solid polymers in 1 mL d_6-DMSO, which were sealed in rectangle quarts cells with 2 mm path length for SANS measurements. The samples were measured with detector distances as 1.15 m, 4.25 m, and 10.25 m, respectively. All these data were further process, reduced, and merged using NCNR SANS package[S20]. The scattering curves were fitted with 2D plate model using SasView[S21].

Conductivity

The conductivity was measured by constructing two types of device as shown in Supplementary Figure S17. The distance of two electrodes in horizontal and vertical measurements were 10 and 1.6 μm, respectively. The current density−voltage (*J*−*V*) profiles were recorded with a Keithley 2400 source meter.

Conductivity measurements of single COF nanosheets

Highly conductive p-silicon wafers (electrical impedance, 0.002 ~ 0.005 Ω mm^{-1}) with 200 nm thermal growth SiO_2 layer were cut into 1 × 1 cm^2 wafer. Hereafter, the wafers were washed twice with chloroform and then cleaned twice by ultrasonication with acetone and ethanol, respectively.

The COF nanosheets were transferred onto the p-silicon wafers from dilute DMI solution, followed by thermal evaporation of the solvents. Two platinum probes were then contact closely with the single COF nanosheets with large area and different thicknesses. The current and voltage were recorded by the semiconductor parameter analyser (keithley 2636B) collecting to the prove system (OYM 130). The micrographs were recorded by Keyence microscope VHX-900F attached to the long work distance lens (VH-Z50L).

Carrier mobility.

The carrier mobility was determined by the TOF method. The device configuration was ITO/COF film (1.637 μm)/Al (300 nm). In TOF experiments, charges were generated by a pulsed nitrogen laser (NL100, SRS, Stanford Research Systems) working at a pulse duration of 3.5 ns and a wavelength of 337 nm. A sourcemeter (Keithley 2400) was used to provide the electric field across the sample. A digital storage oscilloscope (Tektronix MDO3102) was used to record TOF transient signal. The drift mobility was calculated by using the equation $\mu = d^2/(U \times t_{tr})$, where d is the film thickness, U is the applied voltage, and t_{tr} is the transit time taken from the TOF signal curve.

Supplementary Tables

Table S1. Elemental analysis results of PyVg-COF

	C%	H%	N%	Cl%
Calcd.	77.19	4.27	8.18	10.36
Found	75.00	5.16	9.59	10.25

Table S2. Lattice parameters of PyVg-COF

	Eclipsed AA mode	Staggered AB mode
Formula	$C_{176}H_{116}N_{16}Cl_8$	$C_{176}H_{116}N_{16}Cl_8$
Formula weight	2738.58	2738.58
Crystal system	Orthorhombic	Orthorhombic
Space group	CMM2 (No.35)	FMM2 (No.42)
Unit cell dimensions	a = 56.1617 Å, b = 47.5231 Å c = 5.8225 Å $\alpha = \beta = \gamma = 90°$	a = 56.1571 Å, b = 47.8712 Å c = 6.4769 Å $\alpha = \beta = \gamma = 90°$
Cell volume	15540.12 Å^3	17411.90 Å^3
Void space	12925.01 Å^3 (83.17% of unit cell)	12188.73 Å^3 (70.00% of unit cell)

Table S3. Atomistic coordinates for the AA-stacking mode of PyVg-COF optimised by using DFTB+ method (Space group: *CMM2*; $a = 56.1617$ Å, $b = 47.5231$ Å, $c = 5.8225$ Å; $\alpha = \beta = \gamma = 90^{\circ}$)

Atom	*x/a*	*y/b*	*z/c*
H1	0.2874	0.72898	0.57624
H2	0.32025	0.7636	0.57212
H3	0.27374	0.82945	0.73442
H4	0.23937	0.79668	0.75379
H5	0.33544	0.79511	0.36372
H6	0.36931	0.82819	0.34325
H7	0.33794	0.87834	0.87921
H8	0.30465	0.84441	0.91187
N9	0.39498	0.87	0.47748
H10	0.42839	0.86911	0.16444
H11	0.46444	0.89885	0.14593
H12	0.44253	0.9416	0.76282
H13	0.40701	0.91172	0.78667
H14	0.56068	0.97437	0.43532
C15	0.26005	0.76002	0.66292
C16	0.2837	0.75085	0.61587
C17	0.3021	0.76996	0.61159
N18	0.29843	0.79794	0.65653
C19	0.27634	0.80695	0.7217
C20	0.25684	0.78843	0.71128
C21	0.3178	0.81742	0.6408
C22	0.33624	0.81287	0.48097
C23	0.35514	0.83164	0.46726
C24	0.35611	0.85553	0.61041
C25	0.33740	0.86003	0.76706
C26	0.31843	0.8413	0.78355
C27	0.37609	0.87535	0.59854
H28	0.37401	0.89502	0.69994
C29	0.41468	0.8885	0.47308
C30	0.43146	0.88504	0.29512
C31	0.45173	0.90183	0.28469
C32	0.45589	0.92284	0.45013
C33	0.43925	0.9261	0.62909
C34	0.41908	0.90917	0.64217
C35	0.47814	0.93993	0.44311
C36	0.52207	0.96983	0.45167
C37	0.54386	0.98563	0.44567

Cl38	0.21872	0.30975	0.15253
H39	0.5	0.9029	0.42656
C40	0.5	0.92578	0.43228
C41	0.5	0.98489	0.45288

Table S4. Atomistic coordinates for the AB-stacking mode of PyVg-COF optimised by using DFTB+ method (Space group: *FMM2*; *a* = 56.1571 Å, *b* = 47.8712 Å, *c* = 6.4769 Å; *α* = *β* = *γ* = 90˚)

Atom	***x/a***	***y/b***	***z/c***
H1	0.28887	0.22986	0.34761
H2	0.32049	0.26563	0.35251
H3	0.27153	0.33038	0.27349
H4	0.23745	0.29774	0.2861
H5	0.34034	0.29103	0.14073
H6	0.37392	0.3244	0.13413
H7	0.33098	0.38533	0.45094
H8	0.2976	0.35183	0.46662
N9	0.39548	0.36999	0.2151
H10	0.4309	0.36848	0.95087
H11	0.46661	0.39861	0.94753
H12	0.44041	0.44245	0.48198
H13	0.40487	0.41242	0.48746
H14	0.56066	0.47459	0.19736
C15	0.25987	0.26039	0.31682
C16	0.28386	0.25193	0.33496
C17	0.30195	0.27171	0.33386
N18	0.2974	0.29944	0.31196
C19	0.27445	0.30811	0.29416
C20	0.25555	0.28933	0.29806
C21	0.31671	0.31912	0.30516
C22	0.33845	0.31138	0.21329
C23	0.35722	0.33023	0.20721
C24	0.35487	0.35717	0.2926
C25	0.333	0.36467	0.38308
C26	0.31403	0.34598	0.3898
C27	0.37477	0.37706	0.28712
H28	0.37098	0.39843	0.34611
C29	0.41495	0.38862	0.2157
C30	0.43295	0.38474	0.06665
C31	0.453	0.40177	0.06478
C32	0.45593	0.42321	0.2115
C33	0.43813	0.42671	0.36246
C34	0.41799	0.40975	0.36551
C35	0.4781	0.44033	0.21114
C36	0.52209	0.47003	0.21812
C37	0.54385	0.48573	0.20957

Cl38	0.20111	0.81344	0.81433
H39	0.5	0.4036	0.1985
C40	0.5	0.42632	0.20303
C41	0.5	0.48499	0.2202

Table S5. Solubility of PyVg-COF in various solvents

	NMP	DMSO	DMF	DEF	DMAc	DMI
Solubility (mM)	2.2	2.4	2.4	3.0	0.8	1.8
Solubility (mg mL^{-1})	6.2	6.6	6.7	8.3	2.1	4.9

Table S6. Solubility of PyVg-COF in various solvents

COF	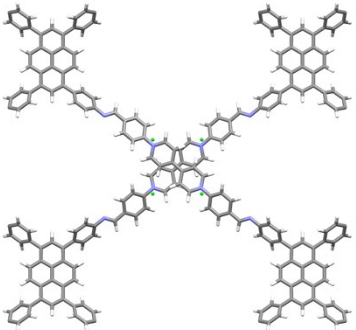 **PyVg-COF with AB stack**	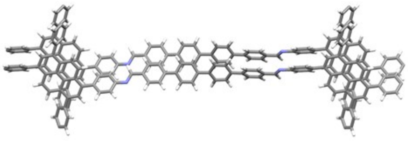 **neutral COF with AA stack**
Interlayer interaction (eV)	2.22	10.45
Interaction with THF (eV)	-1.36	-0.91
Interaction with H_2O (eV)	-1.95	-0.75
Interaction with DMAc (eV)	-4.74	-0.74
Interaction with NMP (eV)	-4.86	-0.75
Interaction with DMF (eV)	-4.87	-0.72
Interaction with DEF (eV)	-5.12	-0.78

Table S7. Conductivity of different COFs reported to date

Materials	**Conductivity ($S\ m^{-1}$)**	**Surface area ($m^2\ g^{-1}$)**	**Ref.**
TTF-COF I_2@TTF-COF TCNQ@TTF-COF	1.2×10^{-4} 1.0×10^{-3} 0.28	720 – –	*Chem. Sci.* **2014**, *5*, 4693; *Chem. Eur. J.* **2014**, *20*, 14614
sp^2c-COF I_2@sp^2c-COF	6.1×10^{-14} 7.1×10^{-2}	692 –	*Science* **2017**, *357*, 673
TTF-Ph-COF I_2@TTF-Ph-COF TTF-Py-COF I_2@TTF-Py-COF	– 10^{-3} – 10^{-4}	1014 – 817 –	*Chem. Eur. J.* **2014**, *20*, 14608
D-A COF	not mentioned, the current was in the nA range	2021	*Adv. Mater.* **2012**, *24*, 3026
COF-366 COF-66	not mentioned, the current was in the nA range	735 360	*Chem. Mater.* **2011**, *23*, 4094
PyVg-COF	0.4	348	**This work**

Supplementary Figures

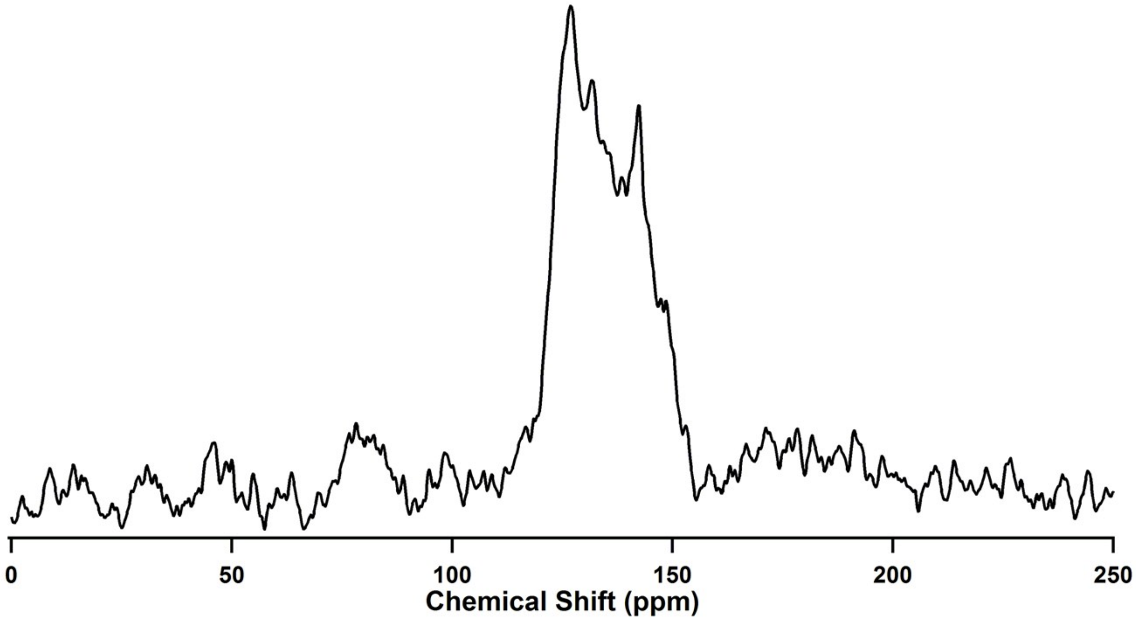

Figure S1. Solid-state ^{13}C NMR spectrum of PyVg-COF.

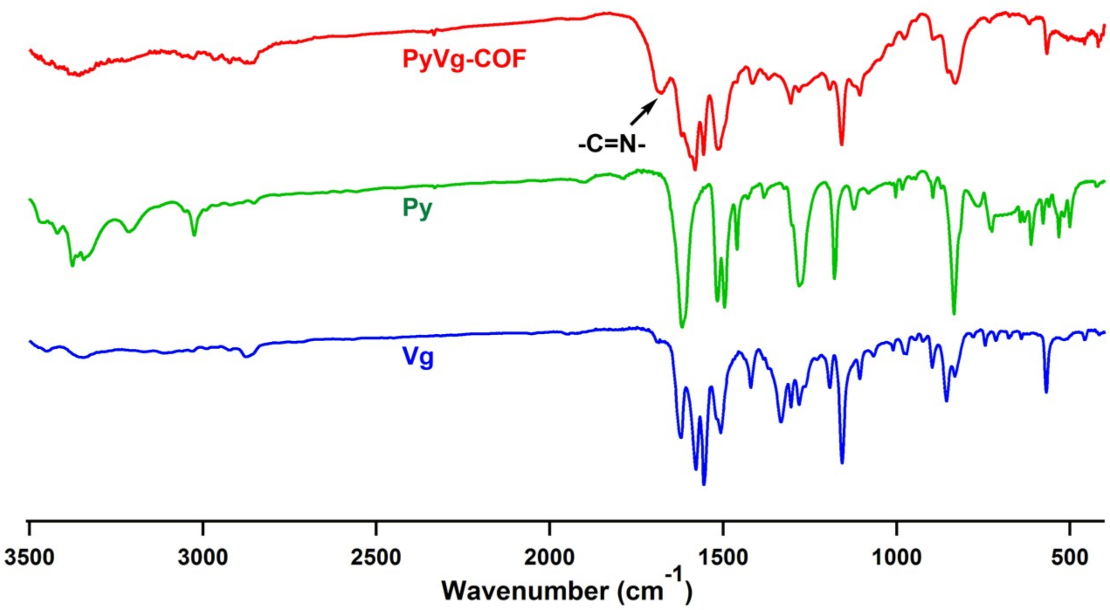

Figure S2. FT-IR spectra of PyVg-COF (red curve), Py monomer (green curve) and Vg monomer (blue curve).

The IR spectra exhibited a newly generated stretching vibration band at 1,681 cm^{-1}, which was assigned to the vibration of C=N bond in imine groups.

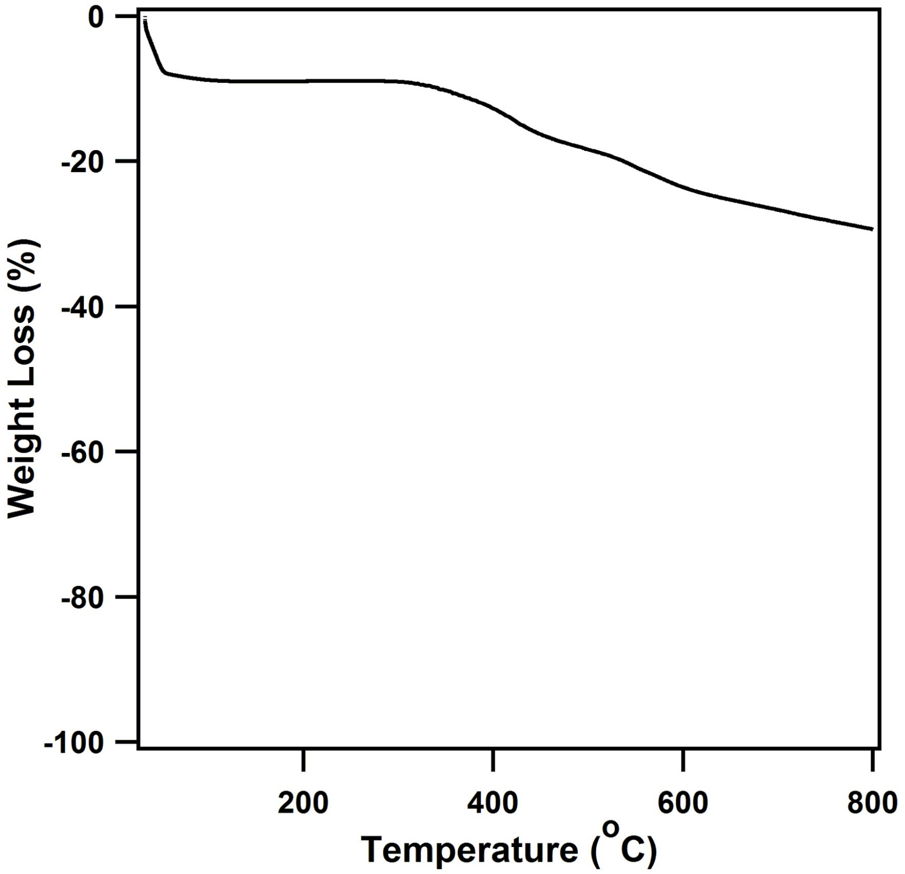

Figure S3. TG curve of PyVg-COF.

The PyVg-COF was stable until 300 °C. At 60 °C the PyVg-COF lost the residual organic solvents (methanol, acetone, THF) in the pores.

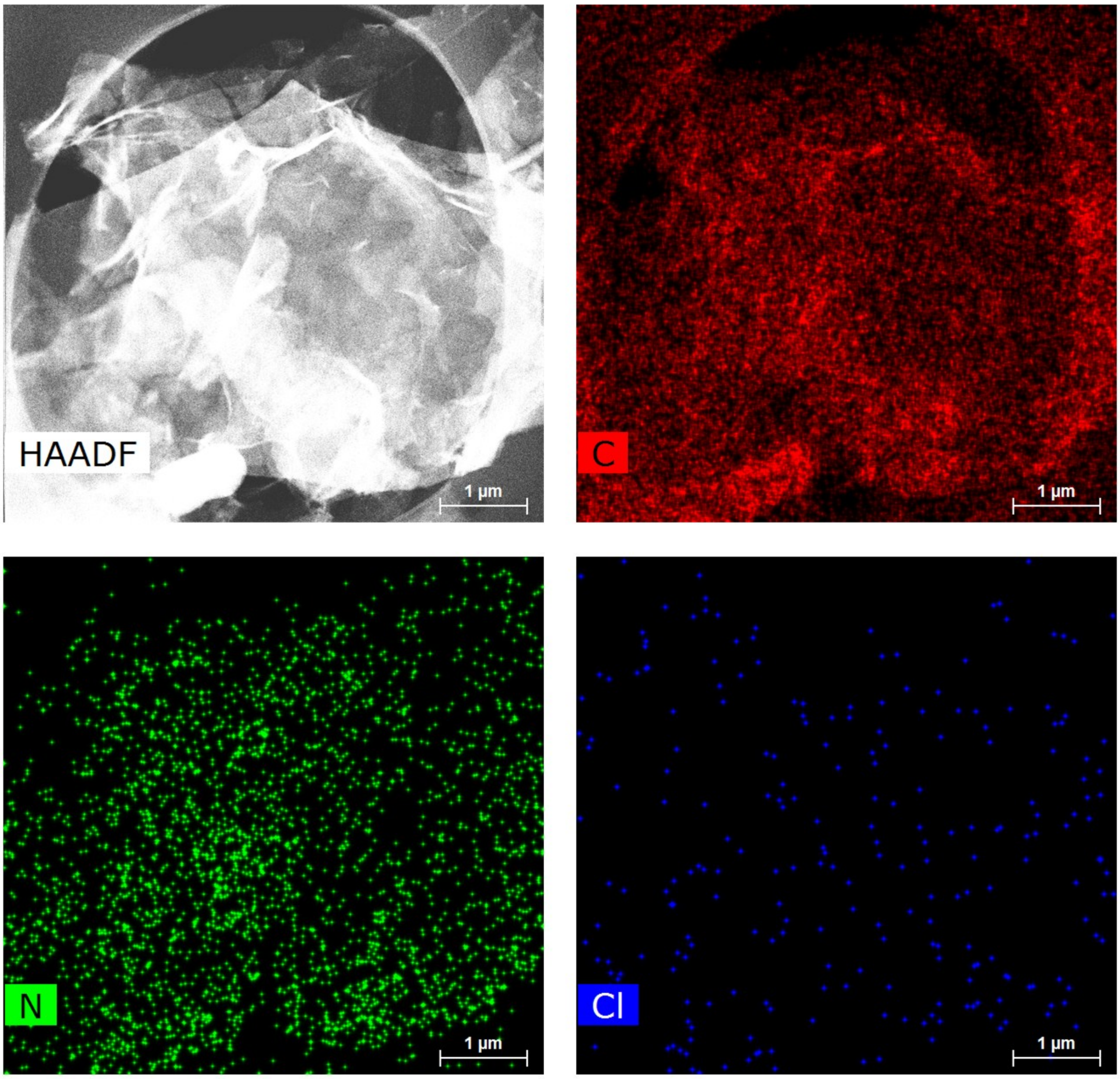

Figure S4. TEM elemental mapping of the PyVg-COF solid. The PyVg-COF showed homogeneous distribution of C, N and Cl elements.

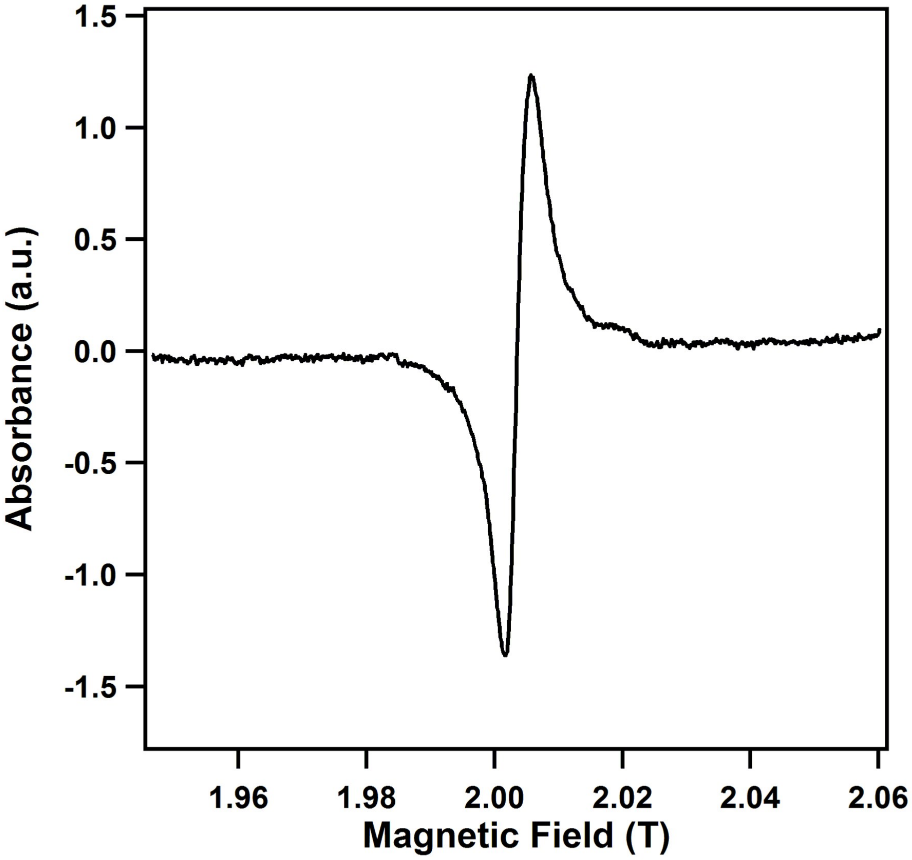

Figure S5. Solid-state electron paramagnetic resonance (EPR) spectrum of PyVg-COF.

The PyVg-COF exhibits an obvious EPR signal. The radical character of the PyVg-COF networks is the result of a charge transfer from the pyrene core to the viologen unit and is an indication of the highly conjugated structures.

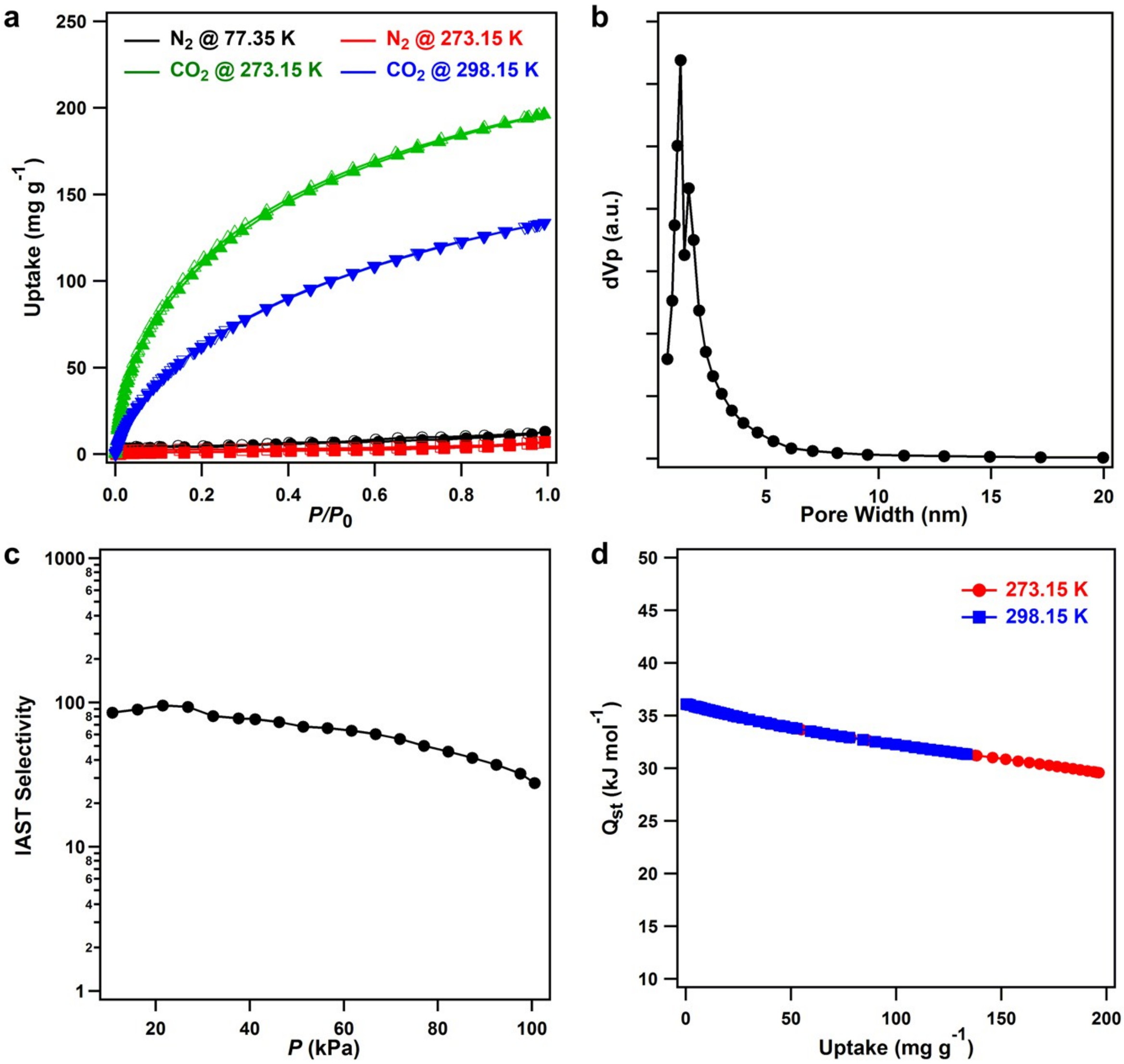

Figure S6. (a) N_2 adsorption isotherm curves at 77.35 and 273.15 K, and CO_2 adsorption isotherm curves at 273.15 and 298.15 K, respectively. (b) Pore size distribution calculated from the CO_2 adsorption isotherm curve at 273.15 K. (c) IAST CO_2/N_2 absorption selectivity of PyVg-COF for the 50/50 CO_2/N_2 flue gas mixture at 273.15 K. (d) Q_{st} curves of CO_2 adsorption at 273.15 and 298.15 K, respectively.

We have calculated the theoretical surface area of our COF material by SAS method, which was 2800 m^2/g. Compared with the theoretical value, the experimental value (348 m^2/g) was obviously small. We speculated that there were two reasons for the small surface area. First, the PyVg-COF adopted AB stack, in which the π-π interactions were much smaller than those in AA stack, and thus gave rise to irregular pore structures. Second, some defects such as non-reacted sites would exist in the COFs. These two factors may significantly decrease the porosity in the COF bulk materials.

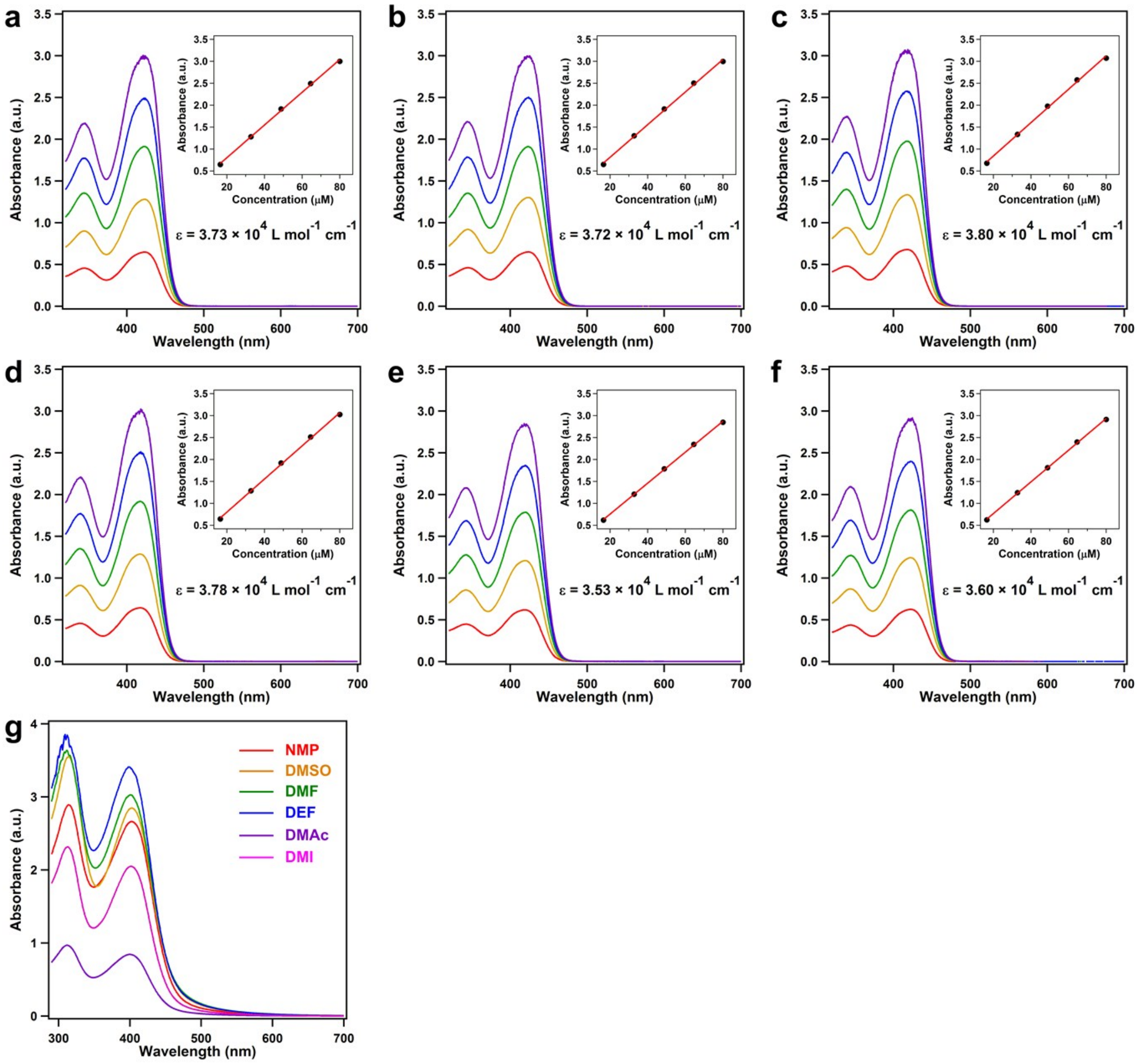

Figure S7. UV-vis spectra of Py monomer in the solvents of (a) NMP, (b) DMSO, (c) DMF, (d) DEF, (e) DMAc, and (f) DMI with different concentrations. (g) UV-vis spectra of PyVg-COF in above-mentioned solvents. The solutions of PyVg-COF for spectral measurements were diluted by 50 folds from the saturated solutions.

The molar absorption coefficient of the 1,3,6,8-tetraphenylpyrene moiety in Py monomers and PyVg-COF was measured by Lambert–Beer's law: $A = \varepsilon \times C \times L$ (A: absorbance, ε: molar absorption coefficient, C: concentration, L: optical length, 1 cm in this case)

From Figure S7a-f we could obtain the ε in different solutions, as was marked in the figures. From Figure S7g we could calculate the concentrations of PyVg-COF in these solvents, and finally get the solubility of PyVg-COF in these solvents under saturated conditions, as listed in Table S3.

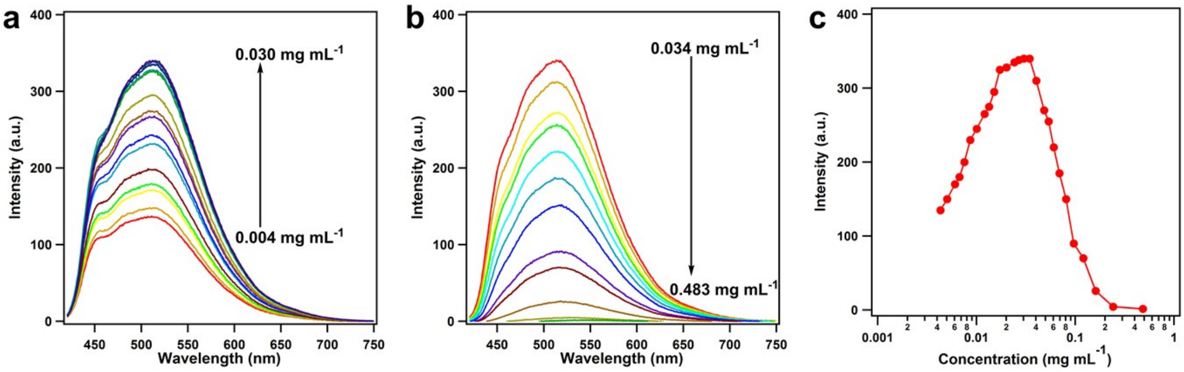

Figure S8. (a) Fluorescence spectra of PyVg-COF NMP solution in the concentration range of 0.004 to 0.030 mg mL^{-1}. (b) Fluorescence spectra of PyVg-COF NMP solution in the concentration range of 0.034 to 0.483 mg mL^{-1}. (c) Relationship of the fluorescence intensity with concentration of PyVg-COF, showing a critical aggregation concentration of 0.034 mg mL^{-1}, under and upon which the nanosheets formed monolayer and submonolayer, respectively.

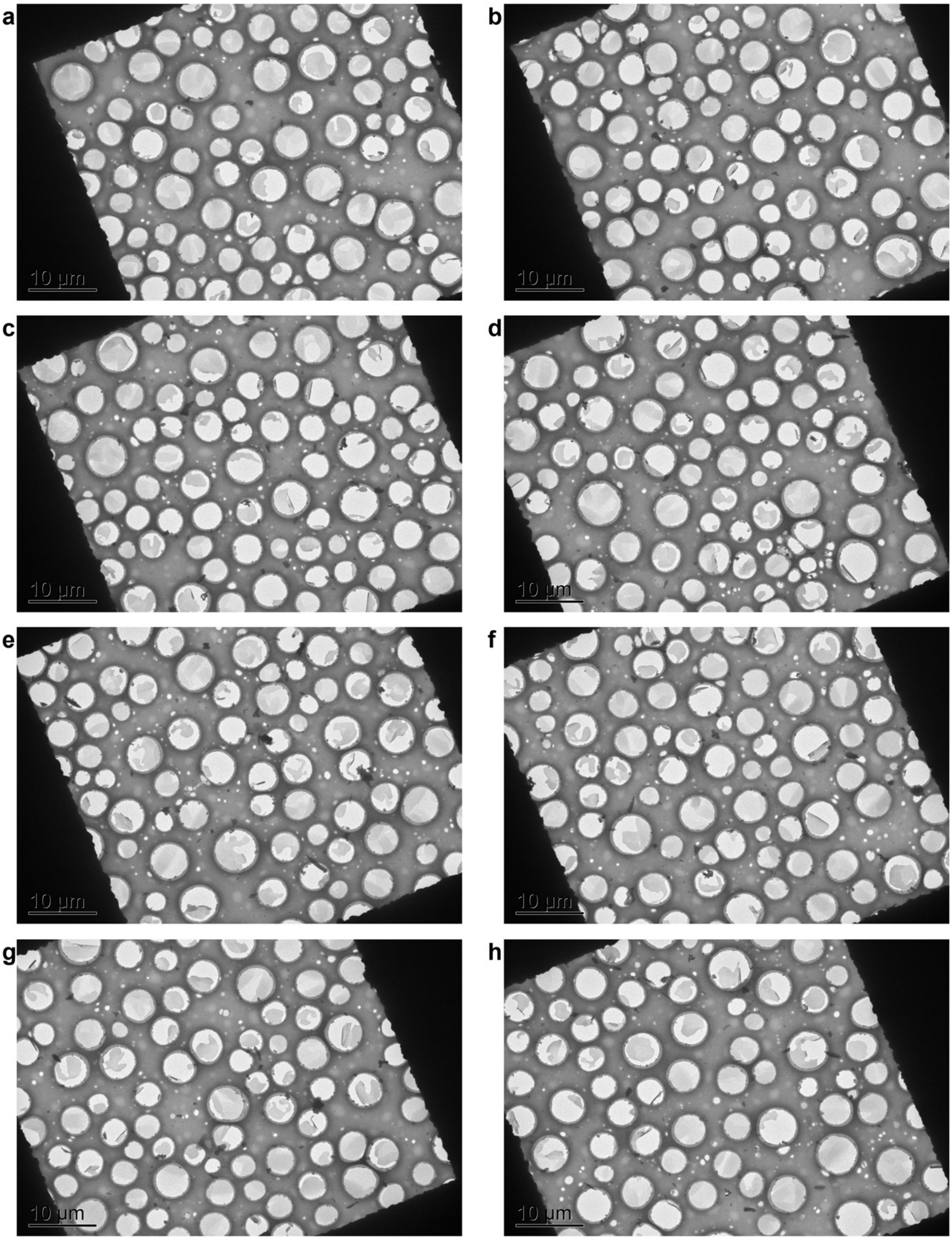

Figure S9. (a) – (h) Randomly obtained TEM images of the PyVg-COF nanosheets at low magnification.

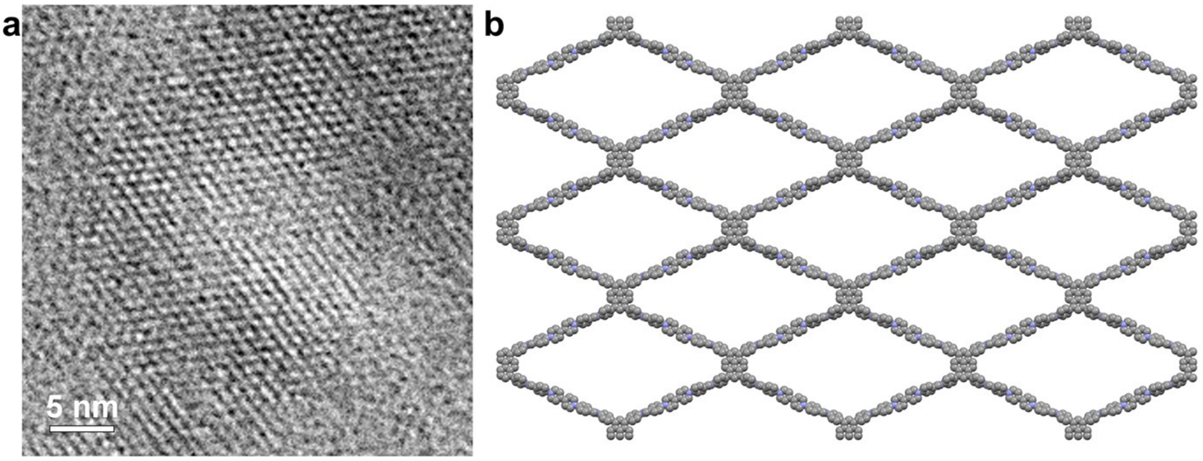

Figure S10. (a) TEM images of the nanosheet of the PyVg-COF at high magnification. (b) Structural simulation of PyVg-COF nanosheets with hexagonal lattice. The H and Cl atoms were ignored for clarification.

Upon further TEM analysis, we were aware that the high-resolution TEM and SAED patterns indicated a hexagonal lattice of the PyVg-COF nanosheets, which was different from that in the bulk powders (orthorhombic lattice). In order to get insight into this phenomenon, we also simulated the hexagonal lattice of the PyVg-COF nanosheets, in which the Py units in the same layer adopted an angle of 60°. This model was also a thermodynamically stable form and well matched with the SAED patterns and high-resolution TEM image. Notably, the angle of the two Vg arms changed from 94° to 120°; the small changes of each Vg arm (13°) could result in global lattice transformation, which originated from the local rotation of C-C bonds neighbouring the imine bonds. Such phenomena were widely recognized in the MOF society as “breathing effect” in various soft MOF materials. Thus, the PyVg-COF exhibited flexibility; it adopted an orthorhombic lattice in the powder state, whereas it transferred into hexagonal lattice in the exfoliated state in the presence of solvents.

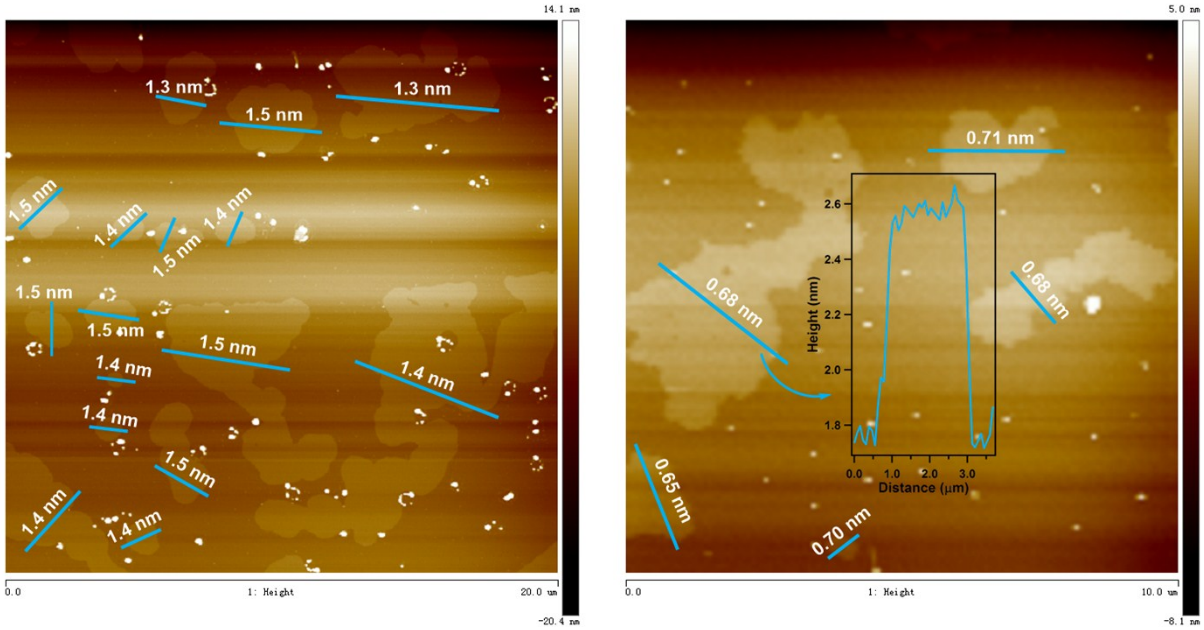

Figure S11. AFM image of PyVg-COF nanosheets deposited from an extremely dilute solution on a mica, followed by thermally evaporating the ethanol solvent. The thickness of the nanosheets ranges from 0.65 nm to 1.5 nm, indicative of the formation of monolayer.

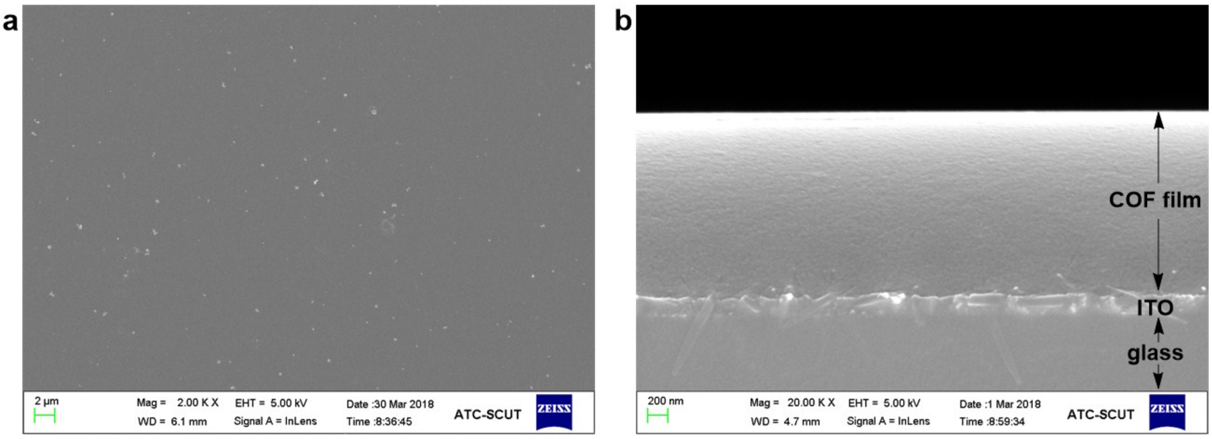

Figure S12. SEM images of (a) the surface and (b) the cross-section of the PyVg-COF films drop-casted from DMI solution on ITO, followed by thermally evaporating the DMI solvent.

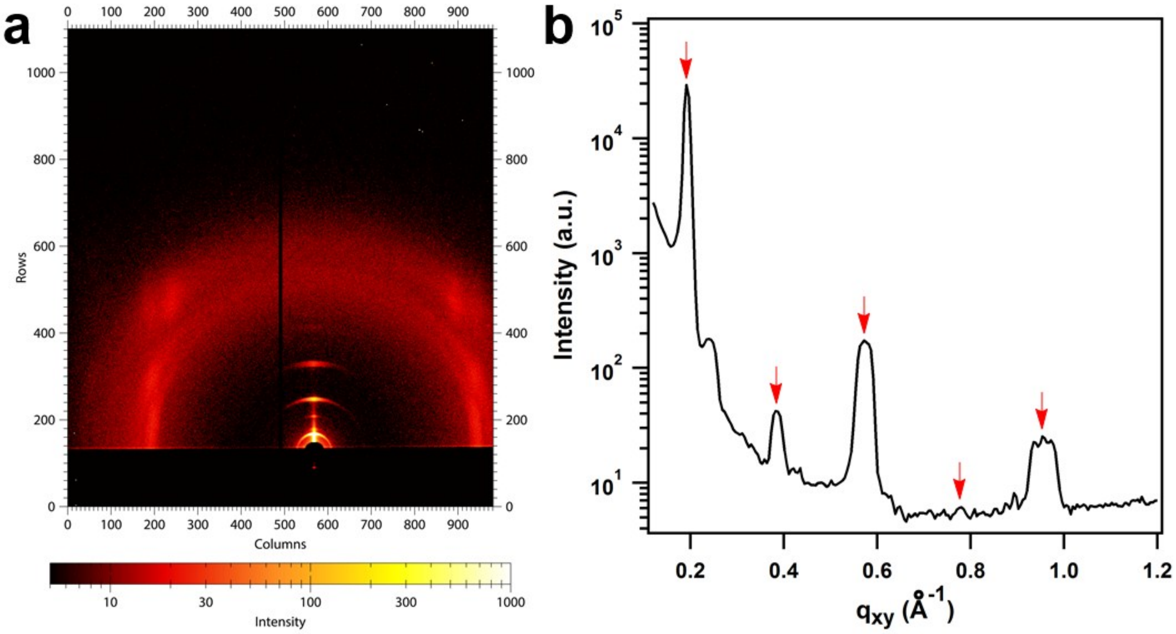

Figure S13. (a) GIWAXS and (b) the out-of-plane diffraction patterns of drop-casted PyVg-COF films.

The drop-casted PyVg-COF films exhibited a typical "face-on" orientation of the COF skeletons to the substrate because the main diffraction patterns located in vertical direction. The diffraction peaks were at 0.19, 0.38, 0.57, 0.78, and 0.95 Å^{-1} (red arrows in Fig. S12b), approximately 1:2:3:4:5, which clearly revealed a 2D layered diffraction mode of the COF films.

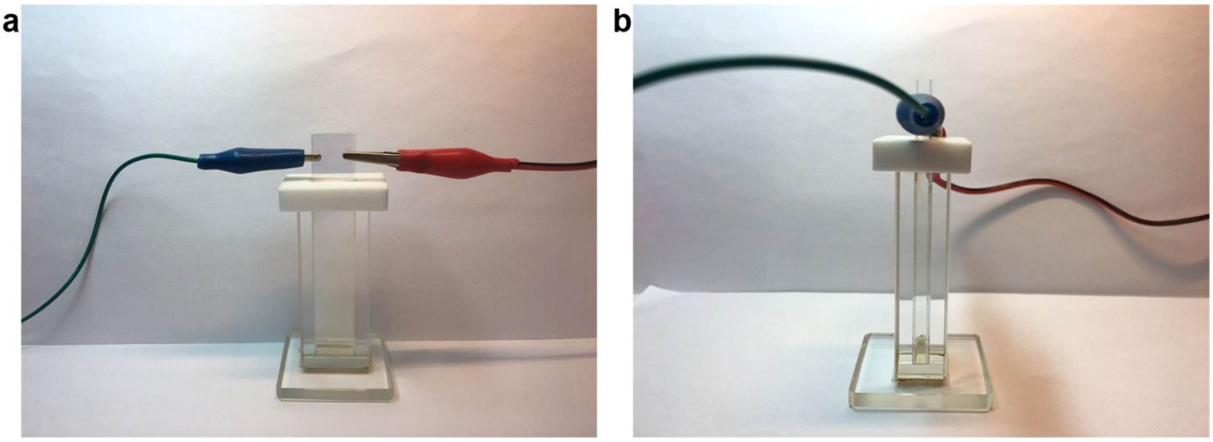

Figure S14. (a) Front view and (b) side view of the EPD setup.

We intentionally designed a special electrochemical cell for EPD process. The inner size of the cell was 60 × 14 × 5 mm^3. In the inner bottom as well as the cover there are respectively two grooves which regulated the distance of the two electrodes to be 3 mm. Considering the EPD rate and the film thickness were positively related with the electric field intensity, this cell design ensured efficient EPD process under a low applied voltage (e.g., 10 V), and enabled the production of thin COF films.

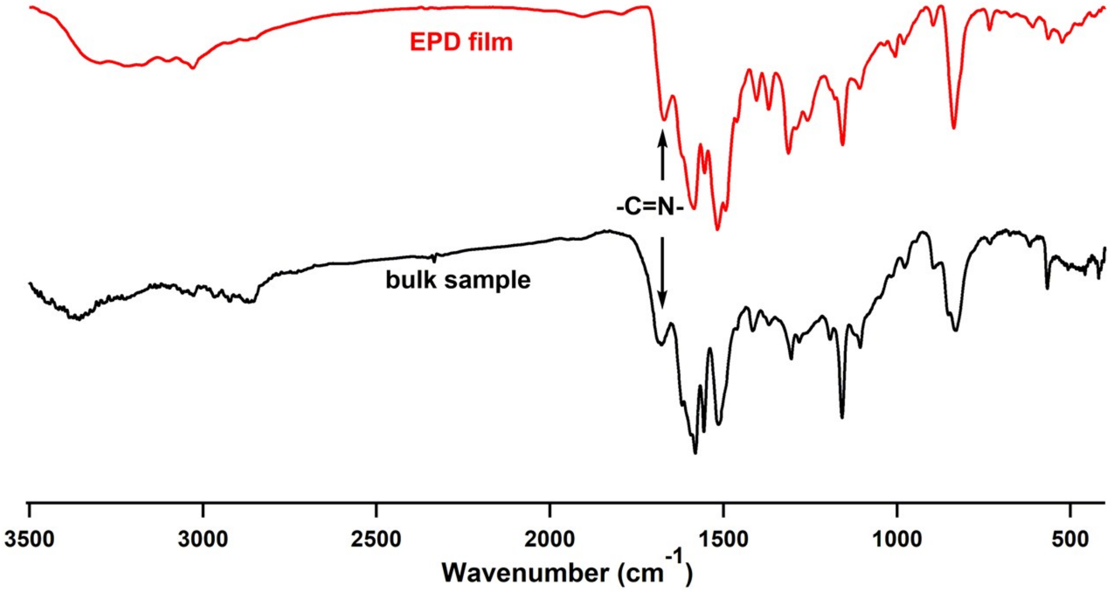

Figure S15. FT-IR spectra of PyVg-COF EPD film (red curve) and bulk sample (black curve).

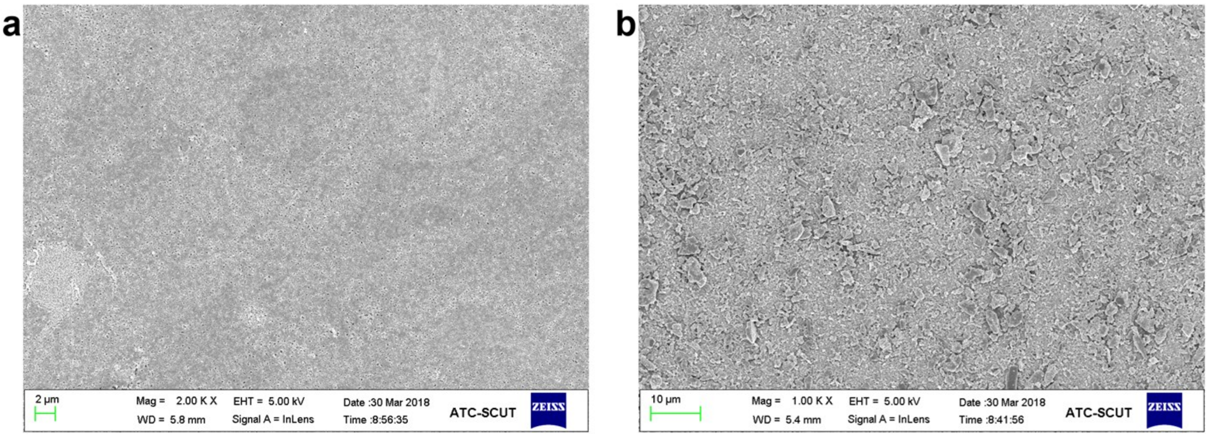

Figure S16. SEM images of PyVg-COF EPD films on (a) ITO and (b) stainless steel electrodes.

SEM image of the films on ITO showed smooth morphology, whereas the films on stainless steel exhibited rough and layered morphology, indicative of oriented structures parallel to the stainless steel substrates.

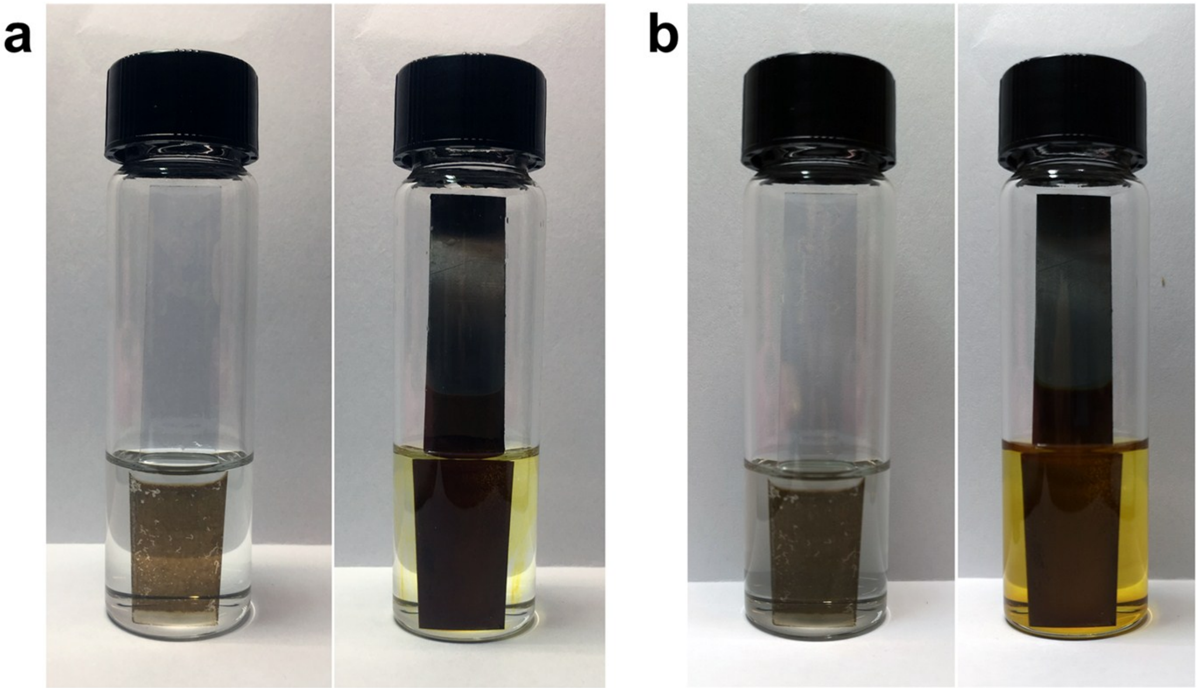

Figure S17. Photos of PyVg-COF EPD films with different thicknesses (left: low thickness; right: high thickness) upon immersing into DMAc for (a) 0 h and (b) 2 h.

We immersed the COF EPD films into DMAc, which is a good solvent for bulk COF sample. When the thickness of the films was low (left photos in both (a) and (b)), the films hardly dissolve in DMAc, which could be attributed to the strong interactions between the COF EPD films and the ITO electrodes. Upon increasing the thickness of the films (right photos in both (a) and (b)), they gradually dissolved in DMAc. These results revealed that the COF EPD films retained their solubility.

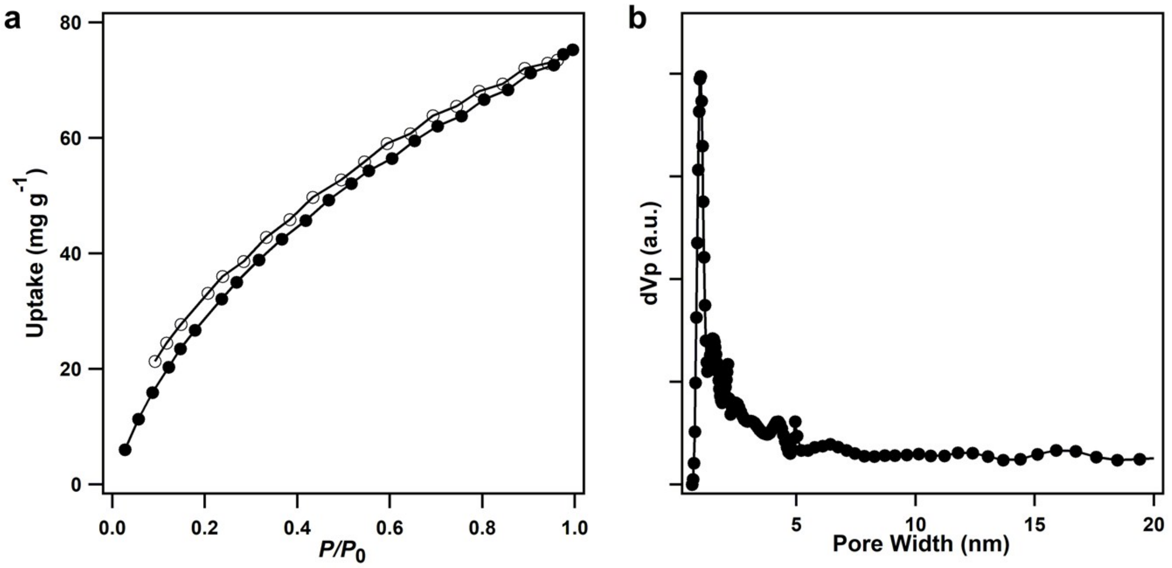

Figure S18. (a) CO_2 adsorption isotherm curves of the EPD films at 273.15 K. (b) Pore size distribution of the EPD films calculated from the CO_2 adsorption isotherm curve at 273.15 K.

The BET surface area of the PyVg-COF EPD films was calculated as 132 m^2 g^{-1}, and the main pore sizes were determined to be 1.0 nm.

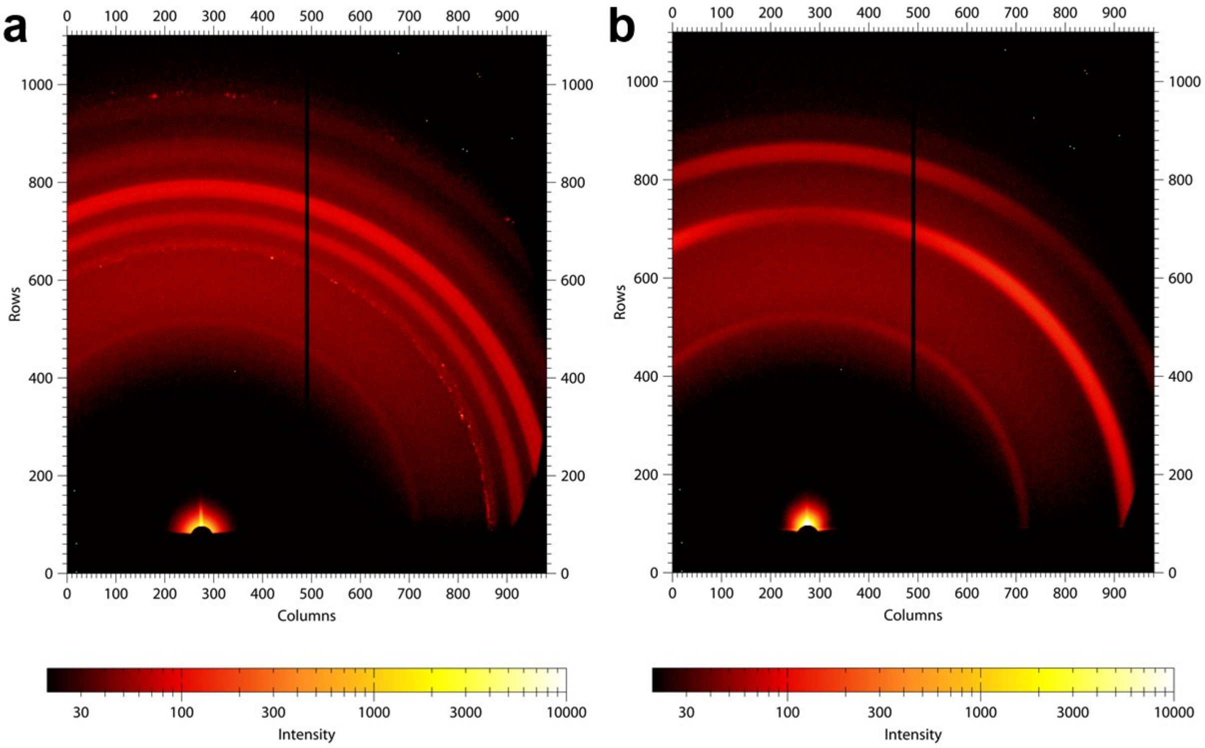

Figure S19. GIWAXS of (a) the PyVg-COF EPD films on ITO and (b) the ITO substrate.

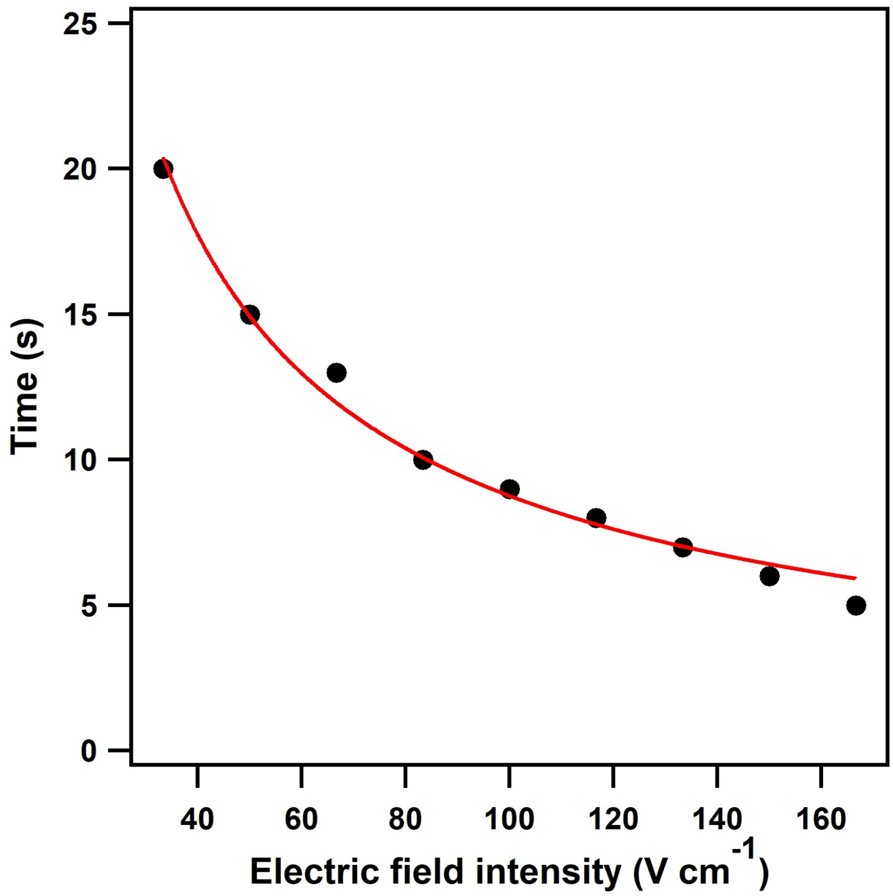

Figure S20. Dependence of the EPD time on the electric field intensity when producing a 70-nm-thick COF film.

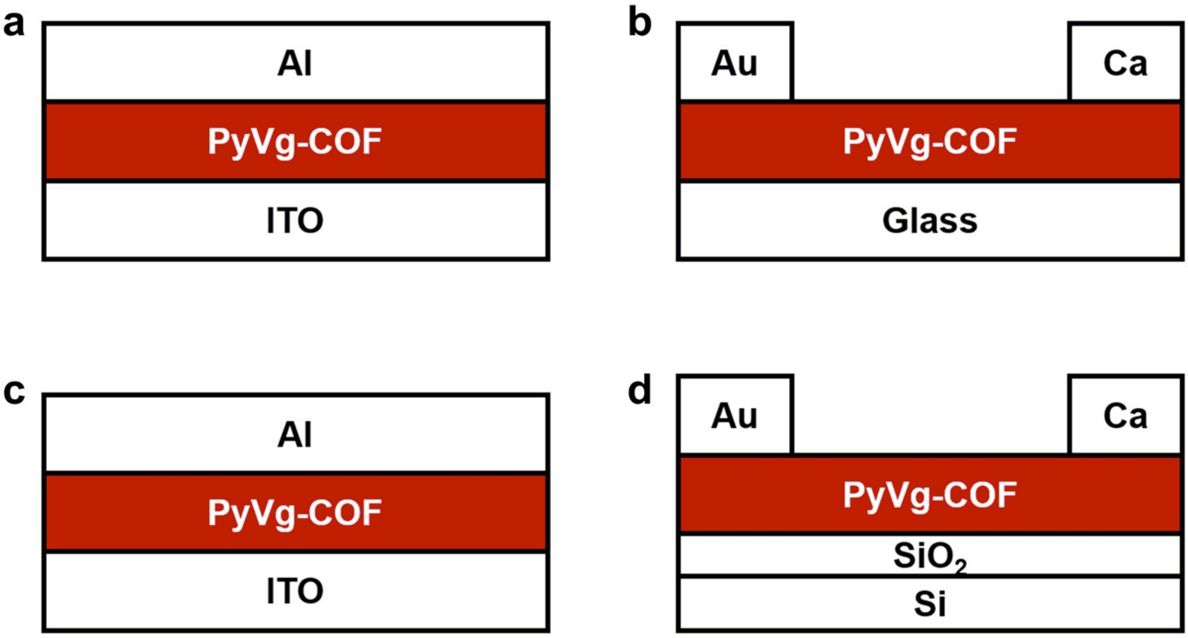

Figure S21. Device structures for measuring the (a) vertical and (b) horizontal conductivity, and the device structures for measuring the carrier mobilities by (c) TOF and (d) FET methods. The thickness of the COF films was 1.6 μm, and the distance between Au and Ca electrodes in (b) and (d) was 10 μm.

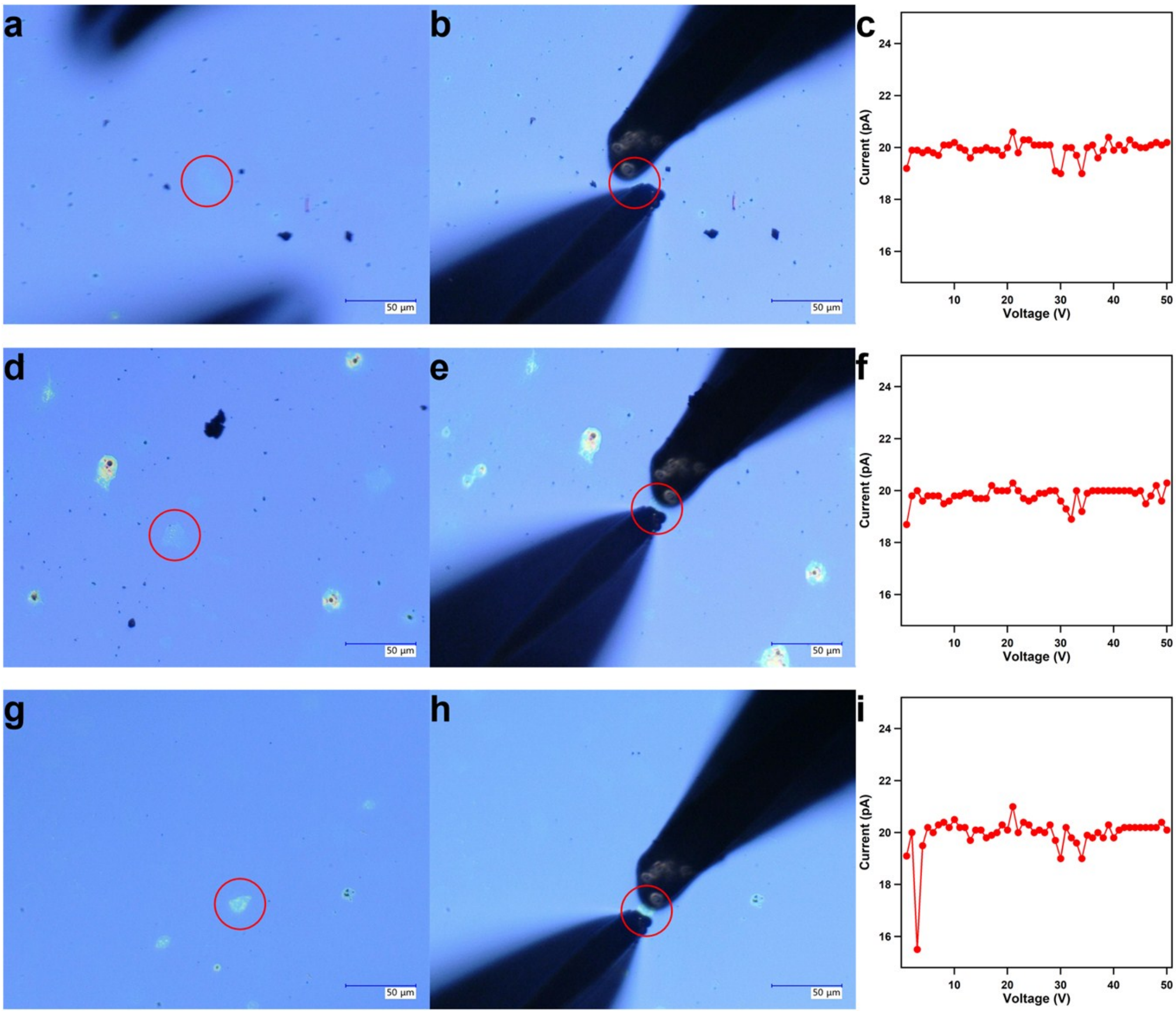

Figure S22. Two-contact probe method to measure the horizontal conductivity of several single COF nanosheets with large area and different thickness. (a)(d)(g) Photos of single COF nanosheets with size of ~ 10 μm. (b)(e)(h) Photos of the two platinum probes contacted with COF nanosheets. (c)(f)(i) The current−voltage profiles of the COF nanosheets.

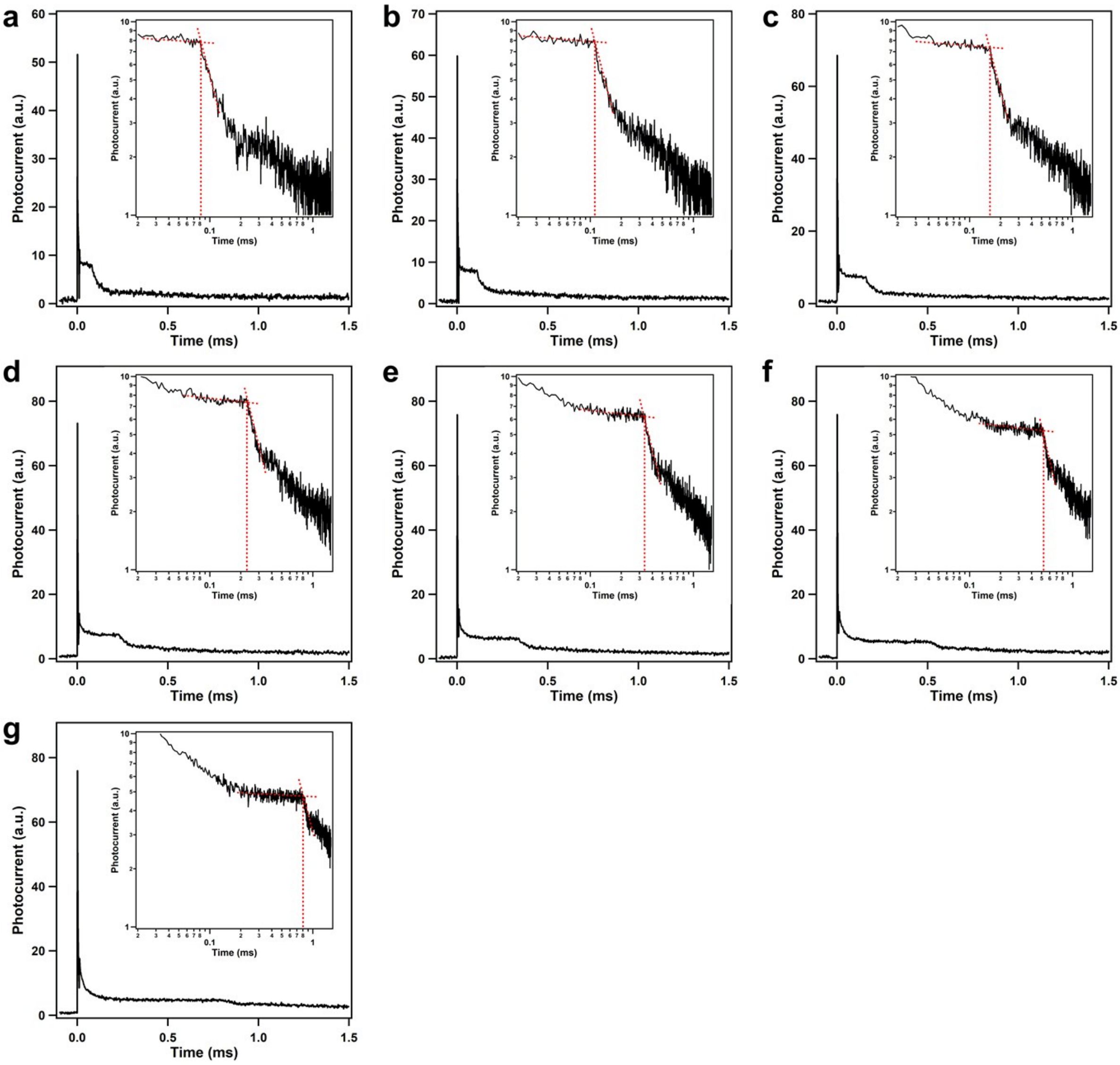

Figure S23. Room-temperature hole photocurrent transient taken at the applied voltages of (a) 50 V, (b) 55 V, (c) 60 V, (d) 65 V, (e) 70 V, (f) 75 V and (g) 80 V. The film thickness was 1.637 µm. Data are plotted in both linear and log–log (inset) scale.

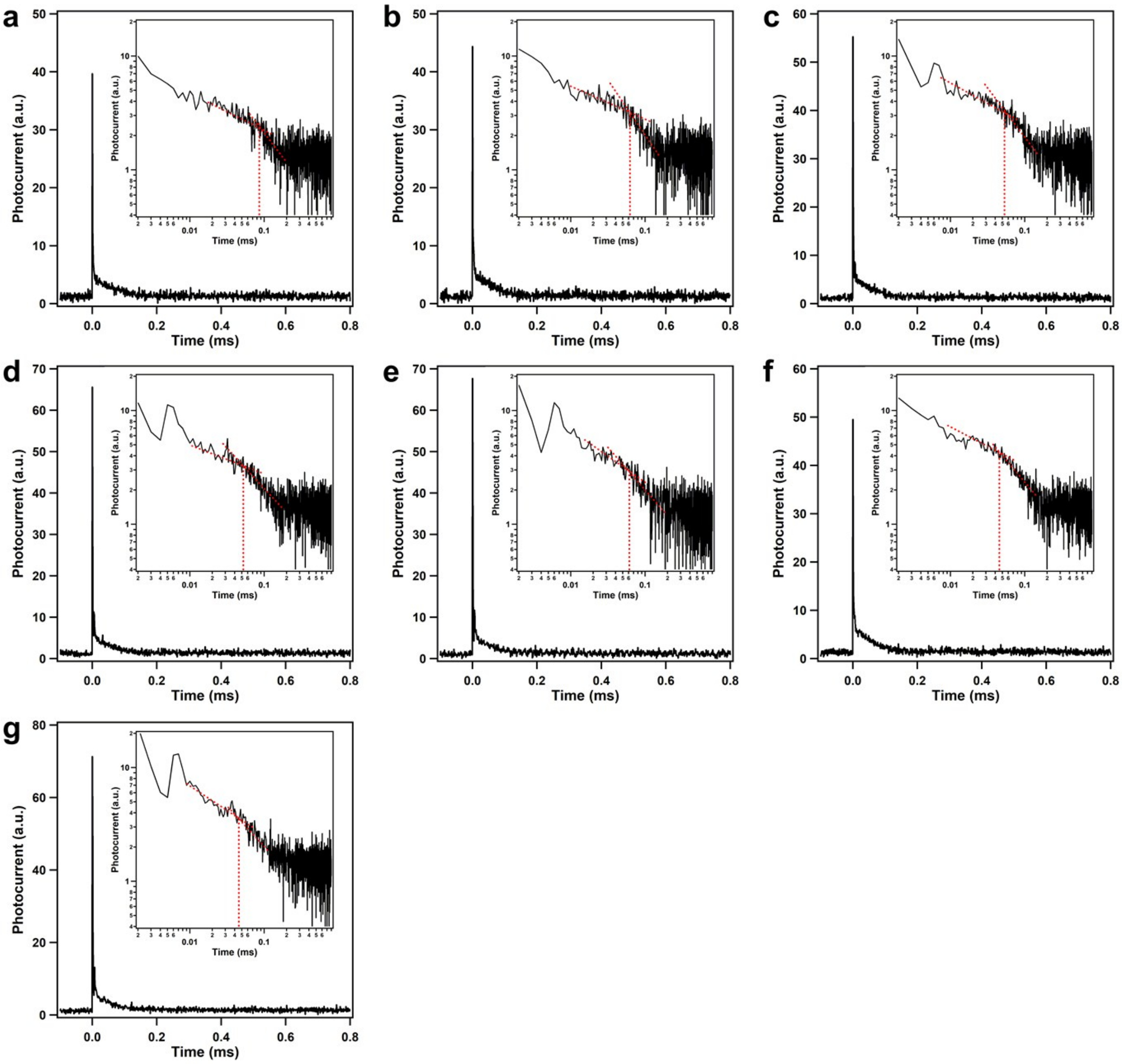

Figure S24. Room-temperature electron photocurrent transient taken at the applied voltages of (a) 30 V, (b) 35 V, (c) 40 V, (d) 45 V, (e) 50 V, (f) 55 V and (g) 60 V. The film thickness was 1.637 μm. Data are plotted in both linear and log–log (inset) scale.

Supplementary References

S1. Huang, N., Chen, X., Krishna, R. & Jiang, D. Two-dimensional covalent organic frameworks for carbon dioxide capture through channel-wall functionalization. *Angew. Chem. Int. Ed.* **54**, 2986−2990 (2015).

S2. Yu, S.-B. *et al.* A polycationic covalent organic framework: a robust adsorbent for anionic dye pollutants. *Polym. Chem.* **7**, 3392−3397 (2016).

S3. http://www.dftb.org.

S4. Aradi, B., Hourahine, B. & Frauenheim, T. DFTB+, a sparse matrix-based implementation of the DFTB method. *J. Phys. Chem. A* **111**, 5678−5684 (2007).

S5. Gaus, M., Goez, A. & Elstner, M. Parametrization and benchmark of DFTB3 for organic molecules. *J. Chem. Theory Comput.* **9**, 338−354 (2013).

S6. Gaus, M., Lu, X., Elstner, M. & Cui, Q. Parameterization of DFTB3/3OB for sulfur and phosphorus for chemical and biological applications. *J. Chem. Theory Comput.* **10**, 1518−1537 (2014).

S7. Kubillus, M., Kubar, T., Gaus, M., Rezac, J. & Elstner, M. Parameterization of the DFTB3 method for Br, Ca, Cl, F, I, K, and Na in organic and biological systems. *J. Chem. Theory Comput.* **11**, 332−342 (2015).

S8. Lu, X., Gaus, M., Elstner, M. & Cui, Q. Parametrization of DFTB3/3OB for magnesium and zinc for chemical and biological applications. *J. Phys. Chem. B* **119**, 1062−1082 (2015).

S9. Dassault Systèmes BIOVIA, D. S. V., Release 2016, San Diego: Dassault Systèmes, 2016.

S10. Kresse, G. & Furthmüller, J. Efficiency of ab-initio total energy calculations for metals and semiconductors using a plane-wave basis set. *Comput. Mater. Sci.* **6**, 15−50 (1996).

S11. Kresse, G. & Furthmüller, J. Efficient iterative schemes for *ab initio* total-energy calculations using a plane-wave basis set. *Phys. Rev. B* **54**, 11169−11186 (1996).

S12. Perdew, J. P., Burke, K. & Ernzerhof, M. Generalized gradient approximation made simple. *Phys. Rev. Lett.* **77**, 3865−3868 (1996).

S13. Grimme, S., Antony, J., Ehrlich, J. & Krieg, J. A consistent and accurate *ab initio* parametrization of density functional dispersion correction (DFT-D) for the 94 elements H-Pu. *J. Chem. Phys.* **132**, 154104-1−154104-19 (2010).

S14. Blöchl, P. E. Projector augmented-wave method. *Phys. Rev. B* **50**, 17953−17979 (1994).

S15. Kresse, G. & Joubert, D. From ultrasoft pseudopotentials to the projector augmented-wave method. *Phys. Rev. B* **59**, 1758−1775 (1999).

S16. Mason, J. A., Sumida, K., Herm, Z. R., Krishna, R. & Long, J. R. Evaluating metal–organic frameworks for post-combustion carbon dioxide capture via temperature swing adsorption. *Energy Environ. Sci.* **4**, 3030−3040 (2011).

S17. Wu, H. *et al.* Cu-TDPAT, an rht-type dual-functional metal−organic framework offering significant potential for use in H_2 and natural gas purification processes operating at high pressures. *J. Phys. Chem. C* **116**, 16609−16618 (2012).

S18. Krishna, R. & van Baten, J. M. Using molecular simulations for screening of zeolites for separation of CO_2/CH_4 mixtures. *Chem. Eng. J.* **133**, 121−131 (2007).

S19. Krishna, R. & van Baten, J. M. *In silico* screening of metal–organic frameworks in separation applications. *Phys. Chem. Chem. Phys.* **13**, 10593−10616 (2011).

S20. Kline, S. R. Reduction and Analysis of SANS and USANS Data using Igor Pro. *J. Appl. Cryst.* **39**, 895−900 (2006).

S21. M. Doucet, *et al.* SasView Version 4.1.2, http://doi.org/10.5281/zenodo.825675.